Electronic Supporting Information

1. Force field validation

Molecular dynamics simulations were performed with the Generalized Amber Force Field (GAFF) and the software NAMD. The dihedral angle between the tetracene and phenyl moieties was parameterized against DFT calculations at PBE0/def2-TZVP level carried out on phenyltetracene using Orca 3.03. The force field was then validated simulating a bulk rubrene crystal supercell. The initial coordinates and lattice parameters were taken from ref.[12]. In more detail, a first MD simulation run in the NPT ensemble was carried out for 10 ns at 300 K, followed by relaxation of 20 ns in the NVT ensemble. The average values extracted from the simulation are reported in Table S1.

Table S1 Comparison between experimental density and unit cell axes and MD simulation results obtained for a 4×2×1 bulk rubrene supercell at 300 K. Unit cell angles were held fixed to the experimental value of 90 degrees.

	a (Å)	**b (Å)**	**c (Å)**	**Density (g/cm^3)**
Experiment	7.17	14.43	26.81	1.27
Simulation (300 K)	7.32	14.15	27.12	1.26
% Difference	**2.0**	**-2.1**	**1.1**	**-0.7**

2. Mechanical properties

A supercell consisting of 256 molecules, with PBC, was equilibrated at constant pressure for 10 ns, then at constant volume for 2 ns. The supercell and the intermolecular distances were then rescaled in order to compress/expand the cell along *a*-, *b*- or *c*-axis and then a final MD run was carried out for 10 ns at constant volume, while recording the pressure profile along the three sides of the box.

Stress (σ) and strain (ε) are related by the stiffness tensor *C*: $\sigma_{ik} = \sum_k \sum_l \ C_{ijkl}\, \varepsilon_{kl}$, where the indices *i, j, k, l* run over the Cartesian axes, here coincident with the lattice unit vectors *a, b, c*. In the absence of shear strain, and by adopting Voigt's notation, it is possible to reduce the stiffness tensor to a symmetric 3 by 3 matrix, $\sigma_{ii} = \sum_k \ C_{ik}\, \varepsilon_{kk}$, so that only six independent elements can be identified.

Two different sets of MD simulations were performed under two different assumptions, represented in Figure *1*b. First, a uniaxial strain was imposed, meaning only one lattice constant of the crystal was rescaled, while the other two were kept constant. The strains to the crystal lattice were imposed by simultaneously modifying one of the supercell box sides and the intermolecular distances along one cell vector *k* while leaving the other directions unaltered ("uniaxial strain" conditions), with values ranging from -0.4% to +0.4% in steps of 0.1%. Stress values σ_{ii} were recorded as the average pressure exerted on three faces of the simulation box.

The three corresponding stress-strain equations for the a, b and c directions become:

$$\begin{pmatrix}\sigma_{aa}\\ \sigma_{bb}\\ \sigma_{cc}\end{pmatrix} = C\begin{pmatrix}\varepsilon_{aa}\\ 0\\ 0\end{pmatrix};\ \begin{pmatrix}\sigma_{aa}\\ \sigma_{bb}\\ \sigma_{cc}\end{pmatrix} = C\begin{pmatrix}0\\ \varepsilon_{bb}\\ 0\end{pmatrix};\ \begin{pmatrix}\sigma_{aa}\\ \sigma_{bb}\\ \sigma_{cc}\end{pmatrix} = C\begin{pmatrix}0\\ 0\\ \varepsilon_{cc}\end{pmatrix} \qquad \text{(S1)}$$

The stiffness tensor elements were computed by fitting each stress-uniaxial strain plot (Figure S1, top) with a line having intercept at (0,0). The angular coefficients of the stress calculated along the direction of strain correspond to the three diagonal elements C_{ii} of the tensor. Off-diagonal elements were derived in a similar fashion, but taking into account the symmetry of the tensor by averaging C_{ij} and C_{ji}. For instance, C_{ba} is calculated as $\sigma_{bb}/\varepsilon_{aa}$ from the simulation where the strain is applied along a, and correspondingly $C_{ab} = \sigma_{aa}/\varepsilon_{bb}$ when strain is applied along b.

Afterwards, the originally non-rescaled sides of each simulation box were then rescaled according to Equation S2, using the calculated stiffness tensor elements to remove the residual off-diagonal strain, thus achieving uniaxial stress conditions. MD simulations of 10 ns were carried out in the NVT ensemble, from which a second series of stress-strain curves was obtained. The uniaxial stress condition implies rescaling the other two lattice vectors previously kept constant in the simulations with uniaxial strain. The three stress-strain systems of equations become thus:

$$\begin{pmatrix}\varepsilon_{aa}\\ \varepsilon_{bb}\\ \varepsilon_{cc}\end{pmatrix} = C^{-1}\begin{pmatrix}\sigma_{aa}\\ 0\\ 0\end{pmatrix};\ \begin{pmatrix}\varepsilon_{aa}\\ \varepsilon_{bb}\\ \varepsilon_{cc}\end{pmatrix} = C^{-1}\begin{pmatrix}0\\ \sigma_{bb}\\ 0\end{pmatrix};\ \begin{pmatrix}\varepsilon_{aa}\\ \varepsilon_{bb}\\ \varepsilon_{cc}\end{pmatrix} = C^{-1}\begin{pmatrix}0\\ 0\\ \sigma_{cc}\end{pmatrix}; \qquad \text{(S2)}$$

where σ_{ii} values were chosen to match the corresponding ε_{ii} for the case of uniaxial strain (i.e. for uniaxial stress along a, σ_{aa} was set to values yielding to ε_{aa}=-0.4%, -0.3%, …, +0.4%, etc.). The trajectories obtained from the two MD series were employed to assess the influence of strain along a, b or c on i) intermolecular degrees of freedom, such as distances and angles, and ii) electronic couplings between rubrene nearest neighbours. The applied strain values and the corresponding cell vectors are summarized in Table S2. The stress-strain curves, calculated for uniaxial stress conditions, are shown in Figure S1 bottom. The correctness of the procedure adopted for the calculations of the stiffness tensor is also shown by the almost flat lines in each plot, corresponding to off-diagonal contributions that were set to zero by imposing a strain calculated from the stiffness tensor.

The Poisson's ratios υ_{ij} can be calculated from the strain tensor elements, which can be rewritten as:

$$C^{-1} = \begin{pmatrix} \frac{1}{E_a} & -\frac{\nu_{ba}}{E_b} & -\frac{\nu_{ca}}{E_c} \\ -\frac{\nu_{ab}}{E_a} & \frac{1}{E_b} & -\frac{\nu_{cb}}{E_c} \\ -\frac{\nu_{ac}}{E_a} & -\frac{\nu_{bc}}{E_b} & \frac{1}{E_c} \end{pmatrix} \qquad \text{(S3)}$$

The Poisson ratio elements of rubrene derived from the results of our MD simulations are reported in Table S3, together with their equivalents calculated from the data in ref. [39]. The higher magnitude of v_{ab} and v_{ba} clearly denotes the high inter-dependency in the strain behaviour existing within the *ab* crystal plane.

Table S2 Summary of applied strain and the corresponding stress values (in GPa) along the three cell axes, together with the dimensions of the unit cell (Å), for uniaxial stress simulations.

ε %	**σ_{aa}**	**a**	**b**	**c**	**σ_{bb}**	**a**	**b**	**c**	**σ_{cc}**	**a**	**b**	**c**
0.4	**-0.036**	7.348	14.100	27.128	**-0.021**	7.304	14.206	27.095	**-0.049**	7.323	14.122	27.226
0.3	**-0.027**	7.341	14.113	27.125	**-0.016**	7.308	14.192	27.100	**-0.036**	7.322	14.129	27.200
0.2	**-0.018**	7.334	14.125	27.123	**-0.011**	7.311	14.178	27.106	**-0.024**	7.321	14.136	27.172
0.1	**0.010**	7.326	14.137	27.120	**-0.006**	7.315	14.164	27.112	**-0.012**	7.320	14.143	27.144
-0.1	**0.010**	7.311	14.162	27.115	**0.006**	7.323	14.136	27.123	**0.012**	7.318	14.157	27.092
-0.2	**0.018**	7.304	14.174	27.112	**0.011**	7.326	14.121	27.129	**0.024**	7.317	14.164	27.064
-0.3	**0.027**	7.297	14.187	27.110	**0.016**	7.330	14.107	27.135	**0.036**	7.316	14.171	27.036
-0.4	**0.036**	7.290	14.199	27.107	**0.021**	7.333	14.093	27.140	**0.049**	7.315	14.177	27.008

Table S3 Calculated and experimental Poisson ratios and Young moduli (GPa) for rubrene.

	calculated, this work	calculated[39]	experimental[40]	calculated[40]
ν_{ba}	0.87	0.82	0.60	0.71
ν_{ab}	0.49	0.60	0.51	0.57
ν_{ac}	-0.12	-0.06	-0.16	0.20
ν_{ca}	-0.09	-0.04	-0.10	0.08
ν_{bc}	0.48	0.21	0.62	0.33
ν_{cb}	0.21	0.09	0.34	0.11
E_a	8.92	9.02	9.01	8.89
E_b	5.12	6.06	7.07	7.14
E_c	11.86	15.17	14.10	21.65

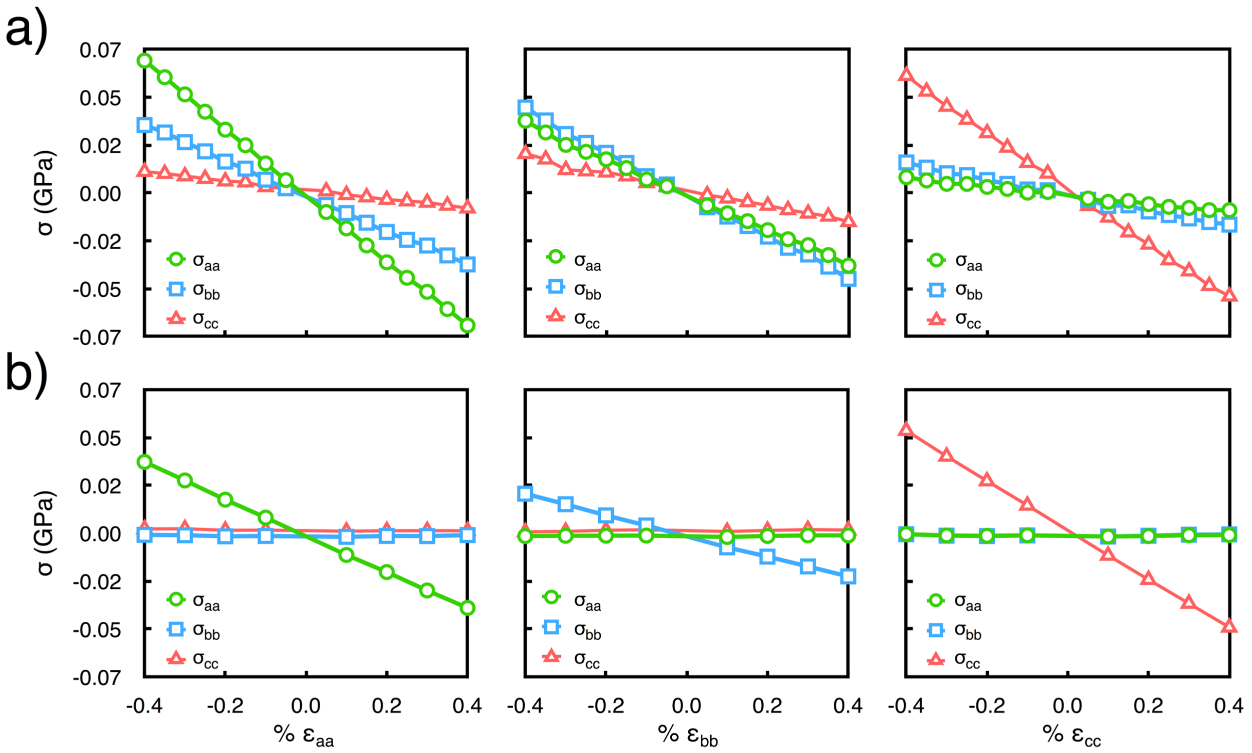

Figure S1 a) plots of applied strain and the corresponding stress values (in GPa) along the three cell axes, for simulations performed at uniaxial strain. b) plots of applied strain and the corresponding stress values (in GPa) along the three cell axes, for simulations performed at uniaxial stress.

3. Analysis of the intermolecular degrees of freedom

In the attempt of rationalizing the strain-induced variation of the electronic couplings J between the nearest neighbours along the a cell vector, relevant intermolecular degrees of freedom were characterized as a function of strain for 1000 snapshot taken from MD simulations along a, b or c, in both uniaxial strain and uniaxial stress conditions. Those included the lateral shift of one molecule along one of its three axes (as shown in Figure S3, Figure S4, Figure S5), and the rotation of one molecule with respect to its three symmetry axes (see Figure S6). In addition, the transfer integral of a dimer taken from the crystallographic structure was calculated while varying the above-mentioned intermolecular coordinates. The comparison between the trends allowed thus to assess the relative importance of each coordinate with respect to the transfer integral variation upon strain.

As far as the rotation angles are concerned, it is shown from Figure S6b and c that, despite a certain dependence of angles θ and χ from strain in the case of uniaxial strain can be found, the absolute variations is always of the order of 10^{-2} degrees. The most sensitive angle with respect to the transfer integral variation is χ, but while J increases with χ, χ increases with positive strain, which in turn was found to decrease J. Instead, transfer integral shows a monotonic decrease with increasing ϕ and θ, although only θ increases slightly with positive strain in the case of uniaxial strain. This brings us to the conclusion that there is not a specific intermolecular mode that can be held solely responsible for the observed variation of mobility with strain.

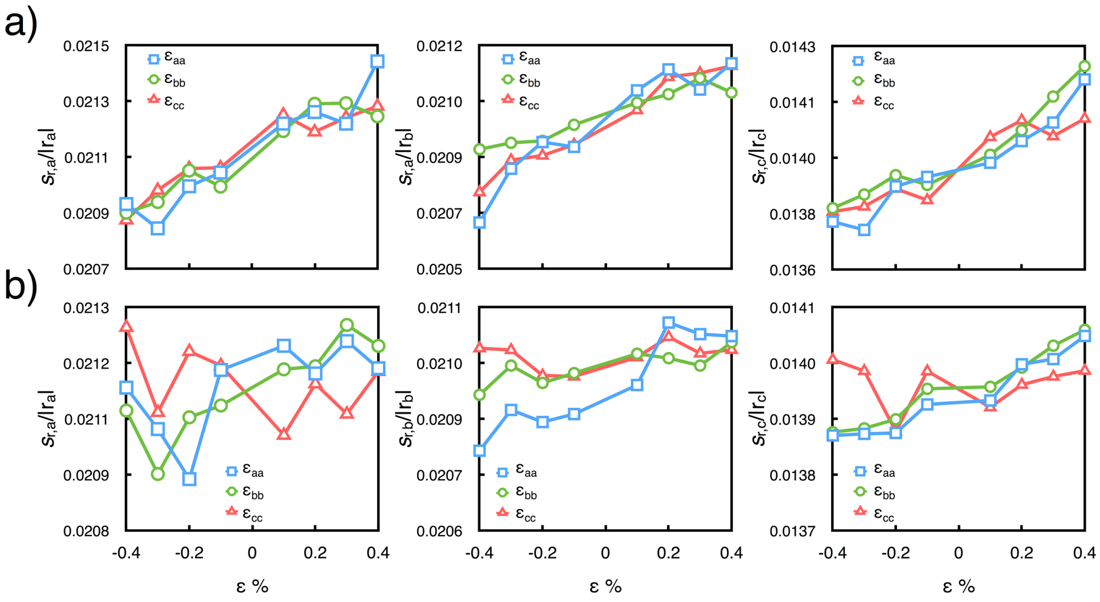

Figure S2 Normalized standard deviations of $|r_a|$, $|r_b|$ and $|r_c|$ for a) uniaxial strain and b) uniaxial stress simulations.

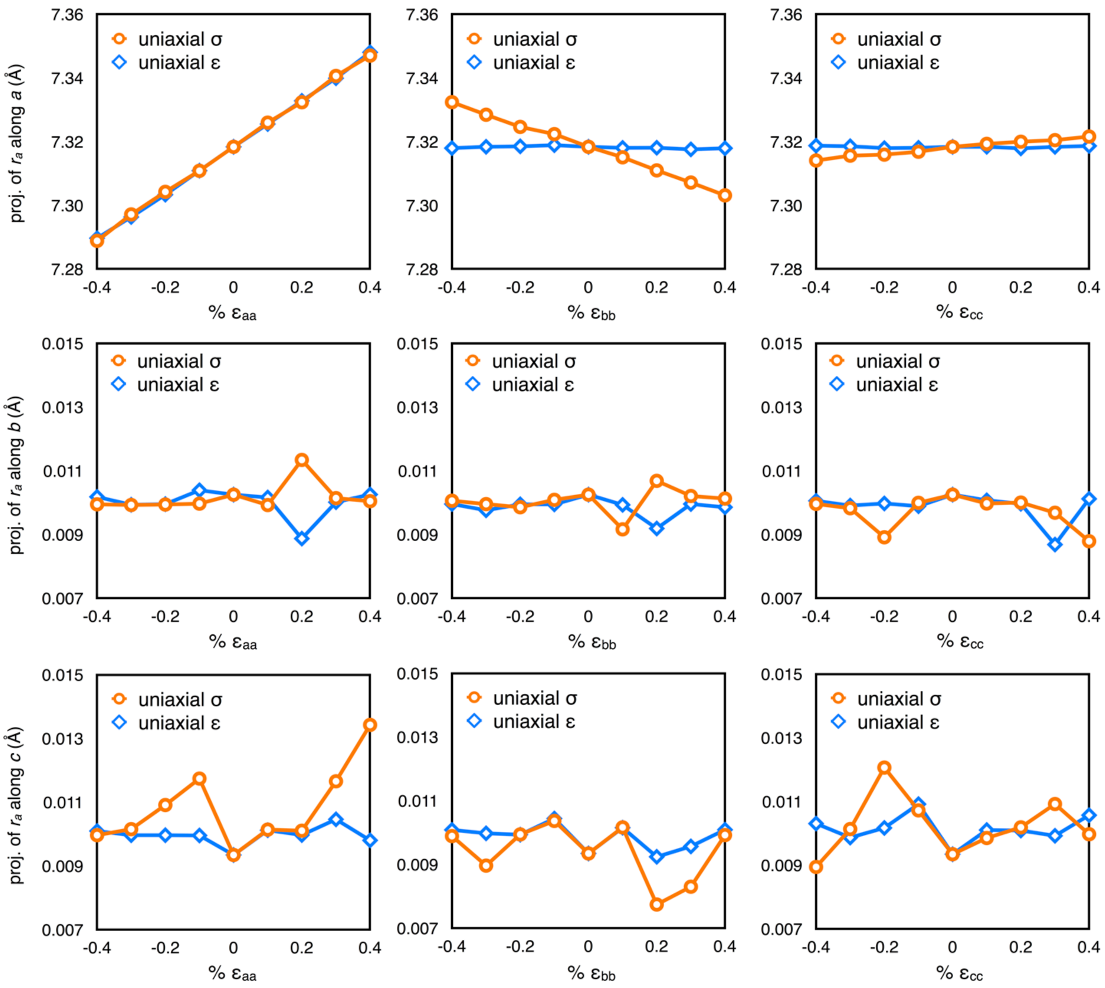

Figure S3 Projection of the interneighbour distance r_a along the three axes as a function of strain

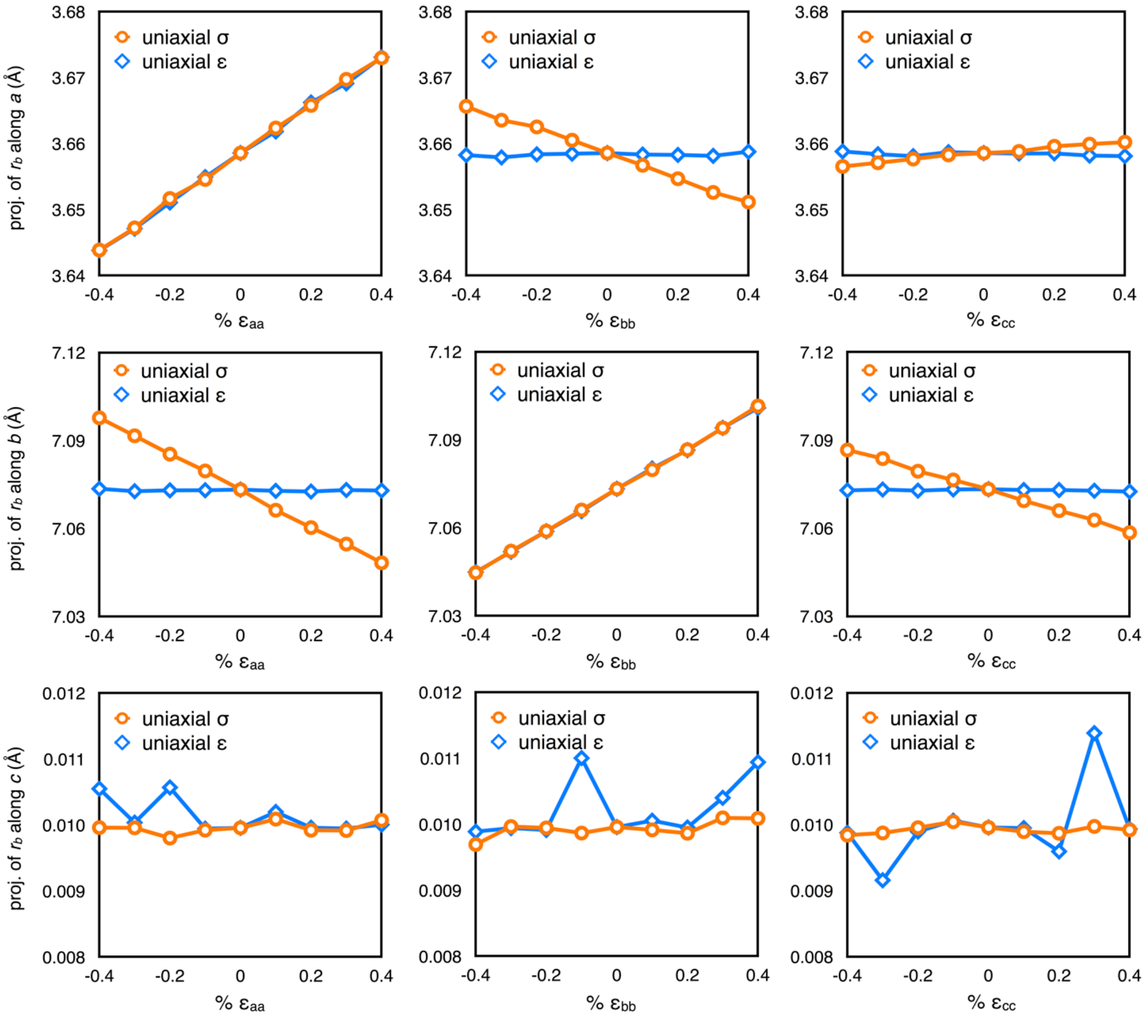

Figure S4 Projection of the interneighbour distance r_b along the three axes as a function of strain.

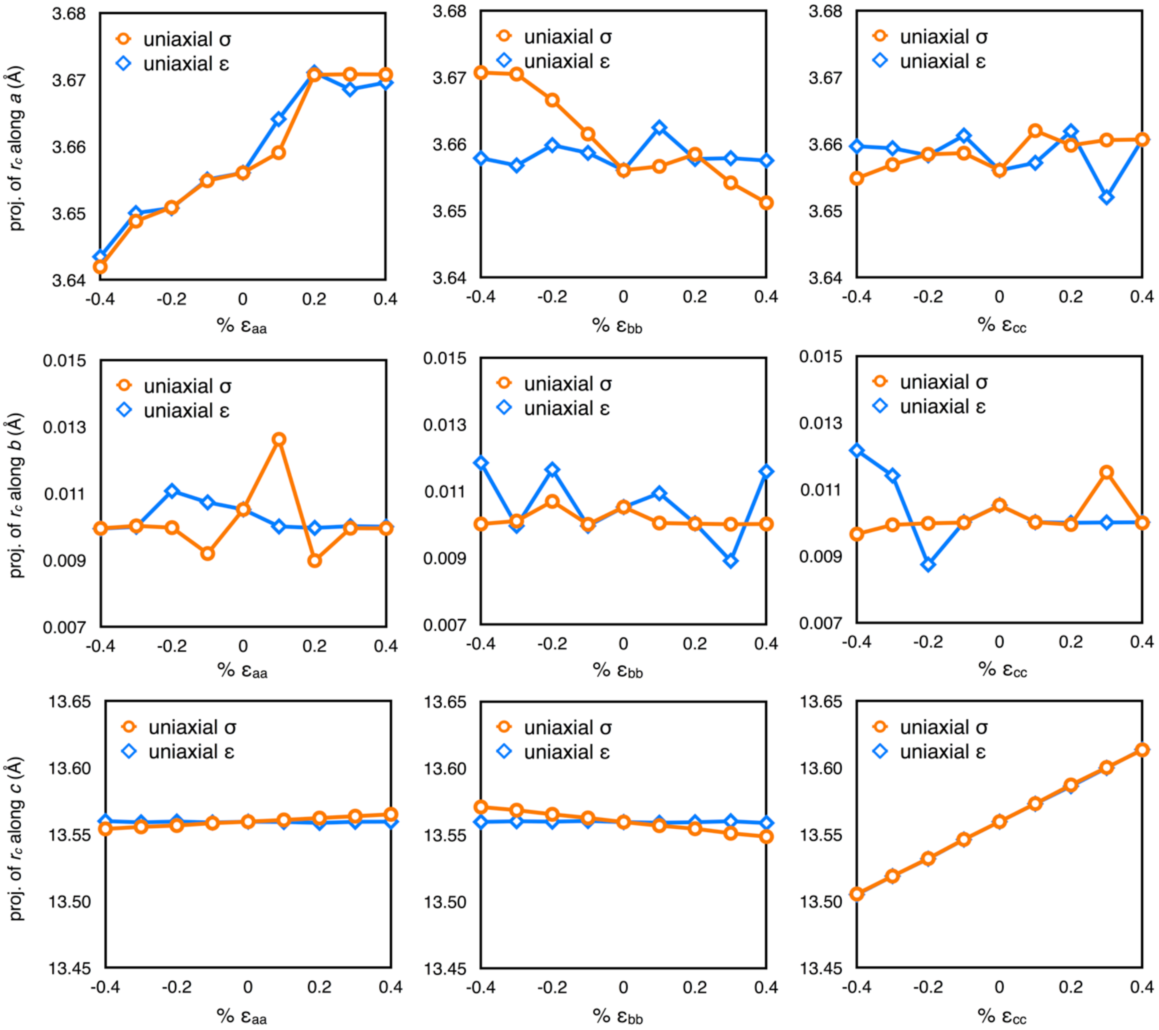

Figure S5 Projection of the interneighbour distance r_c along the three axes as a function of strain.

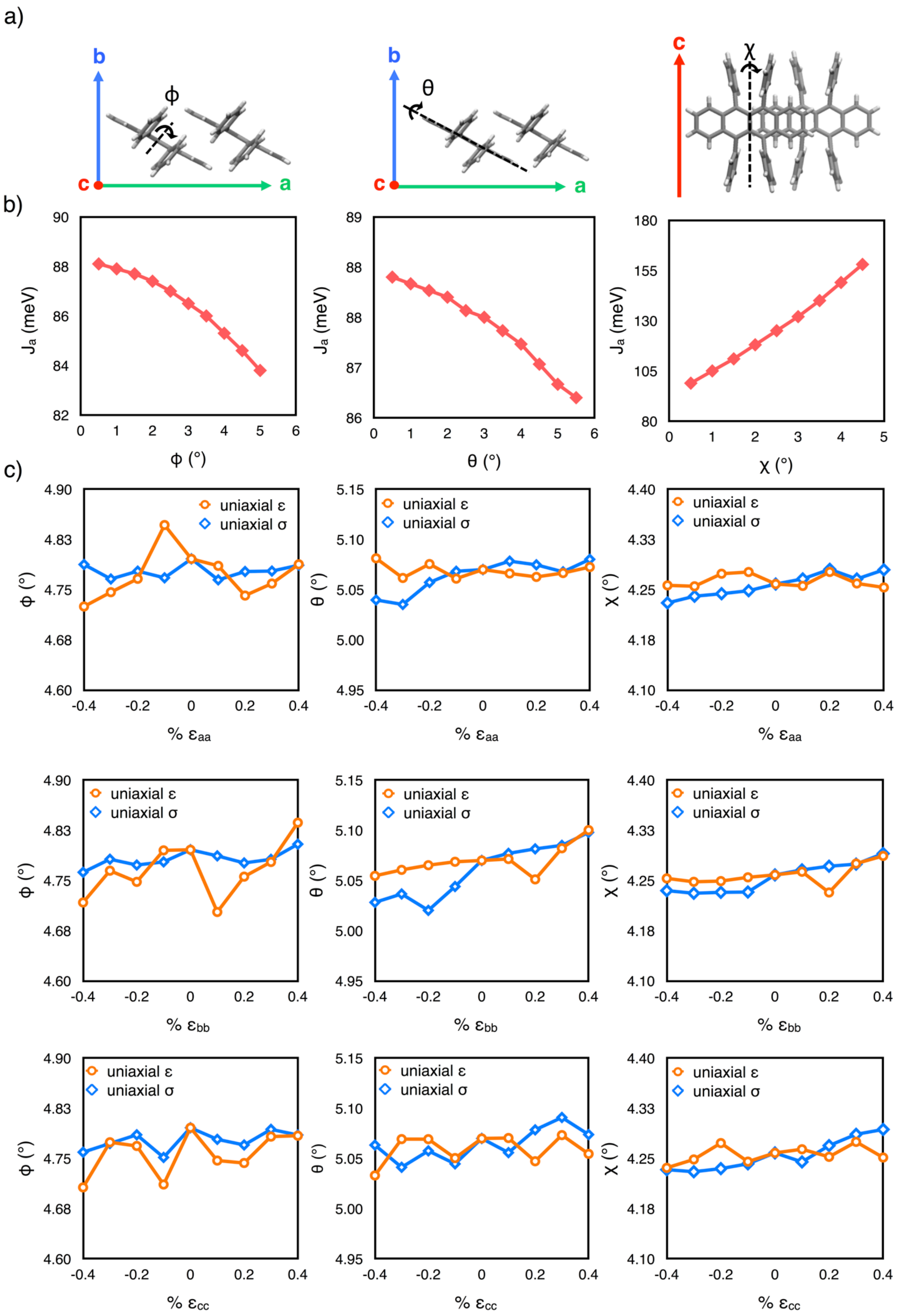

Figure S6 a) Visual representation of ϕ, θ and χ. The rotation direction with respect to the symmetry axes (dashed lines) is shown by the black arrows. b) Variation of J_a as a function of ϕ, θ and χ, calculated from a dimer extracted from the crystal unit cell in the absence of strain. c) Variation of ϕ, θ and χ as a function of strain, extracted from MD simulations.

Table S4 Average values of J_a and J_b transfer integrals calculated with ORCA and the projection method at different levels of theory, for simulations with uniaxial mechanical strain applied along b. Corresponding relative linear and quadratic variations with respect to the unperturbed single crystal are also given. DFT and Z stand for B3LYP/6-31G* and ZINDO calculations at the MD geometries. OPT-Z stands for ZINDO calculations on AM1-optimized geometries in which bond lengths and angles were relaxed. Calculations at zero strain with the ADF suite yield J_a=0.0881 using the B3LYP functional and the DZ basis set.

ε_{bb} %	quantity	*a*, DFT	*a*, Z	*a*, OPT-Z	*b*, DFT	*b*, Z	*b*, OPT-Z
-0.40	transfer integral J_i (eV)	0.1059	0.0969	0.0968	0.0161	0.0109	0.0109
0.00		0.1036	0.0936	0.0935	0.0157	0.0105	0.0105
0.40		0.1012	0.0904	0.0902	0.0153	0.0101	0.0101
-0.40	relative variation $(J_i-J_{i0})/J_{i0}$ %	2.28	3.50	3.52	2.68	3.88	3.80
0.00		0.00	0.00	0.00	0.00	0.00	0.00
0.40		-2.27	-3.50	-3.49	-2.40	-3.63	-3.70
-0.40	relative square variation $(J_i^2- J_{i0}^2)/J_{i0}^2$ %	4.61	7.12	7.17	5.43	7.91	7.75
0.00		0.00	0.00	0.00	0.00	0.00	0.00
0.40		-4.50	-6.88	-6.86	-4.73	-7.13	-7.26

4. Distribution of transfer integrals calculated from selected MD snapshots

To derive the shape of the distribution of electronic coupling, which reflects the distribution of intermolecular degrees of freedom, a total of 34 300 ps-spaced frames from the 10 ns simulation time were extracted and electronic couplings were calculated for every dimer in the simulation supercell along *a*, *b* and *c*. They are hereby called $|J_a^t|$, $|J_b^t|$ and $|J_c^t|$ in order to distinguish them from the electronic couplings calculated from a single averaged configuration reported in the main discussion of this work). Due to the huge number of calculations required, the cheap and cost-effective ZINDO Hamiltonian was used in all the calculations. The comparison with DFT values reported in Table S4 indicate that ZINDO captures both the correct order of magnitude of the couplings and of their variation upon strain, with respect to more expensive DFT calculations, and that the underestimation of C=C bond length alternation typical of the GAFF force field is unimportant for what concerns the transfer integral calculation.

The distributions of the electronic couplings at different strain values (0, +0.4% and -0.4% along *a*, *b* and *c* are reported for MD simulations performed in both uniaxial stress and strain conditions, respectively in Figure S7 and Figure S8Additional data about the distributions for the whole strain interval analysed in this work are also reported in *Table S4*. The distributions have a slightly skewed Gaussian shape, whose standard deviation remains mostly unchanged upon positive or negative strain. The changes in the maximum and average $|J_a^t|$, $|J_b^t|$ and $|J_c^t|$ reflect the trends already observed in Figure 2 and commented in the main text of this article.

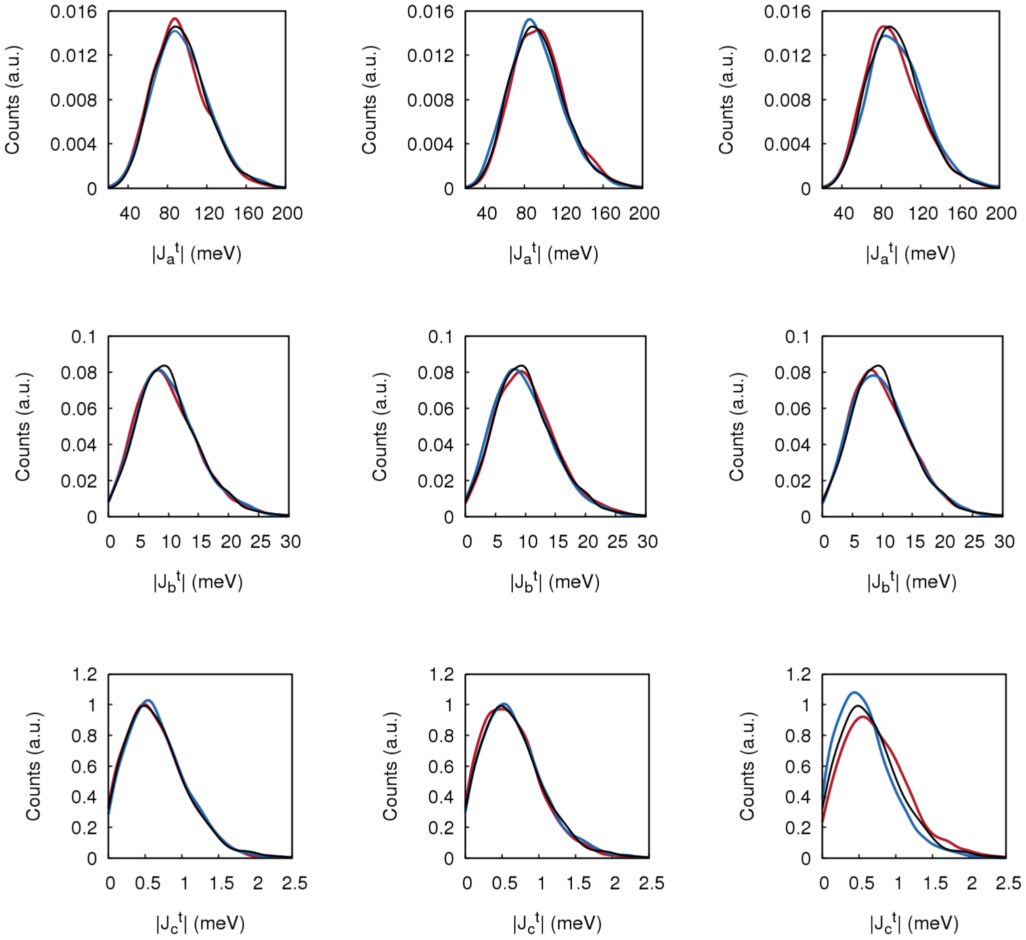

Figure S7 Normalized distributions of the instantaneous values of the transfer integrals a) $|J_a^t|$*, b)* $|J_b^t|$ *and c)* $|J_c^t|$ *calculated for ε=0 (black line), +0.4% (blue line) and -0.4% (red line), in uniaxial stress conditions. From left to right, strain is applied along a, b, and c, respectively.*

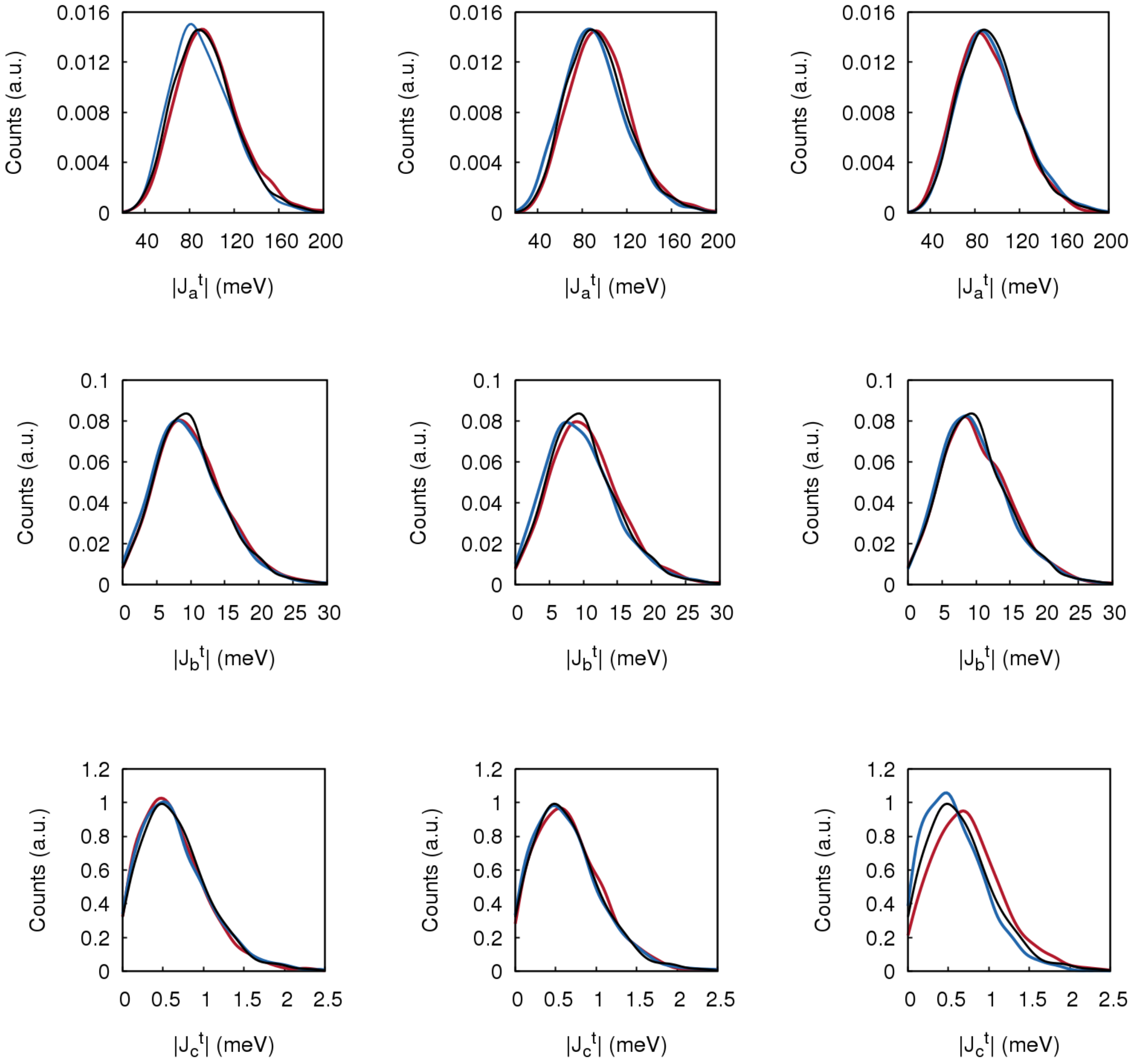

Figure S8 Normalized distributions of the instantaneous values of the transfer integrals a) $|J_a^t|$*, b)* $|J_b^t|$ *and c)* $|J_c^t|$ *calculated for ε=0 (black line), +0.4% (blue line) and -0.4% (red line), in uniaxial strain conditions. From left to right, strain is applied along a, b, and c, respectively.*

5. Strain and mobilities along c.

Hole mobilities were evaluated using a hopping model, where $\Delta\mu_i^\varepsilon$ is found to be proportional to the square of the transfer integral J_i^2 (see Equation 5 in the article). The variation of mobility along c, hard to measure experimentally, appears to be the most sensitive when compression/tension along *c* is applied (Figure S9). $\Delta\mu_c^c$ in this case reaches 60% and follows the expected decreasing trend with strain, as reflected by the large *m* values in Table *2*. In case of deformation along *a* and *b*, the mobility measured along *c* is less perturbed, and in particular it hardly changes upon a stress applied along *a*. This is clearly related to the corresponding Poisson ratios: since ν_{cb} and ν_{ca} are relatively small, deformations along *a* and *b* are not expected to produce large effects on the arrangement of rubrene molecules along the out-of plane direction *c*. We note that our results for the mobilities along c may be partial because only one type of neighbour along c was considered (see reference[43] for details).

The effect of a *c* strain on the mobility along *b* has the expected decreasing trend with a response very similar to the one to the stress along *b*. We predict instead for mobilities along a an increase with tensile strain applied along *c*, in particular for uniaxial stress conditions, and the same trend for mobility measured along *c* upon stress application along *a* (Figure S9ac and ca), in accord with the negative Poisson's ratios ν_{ac} and ν_{ca}.

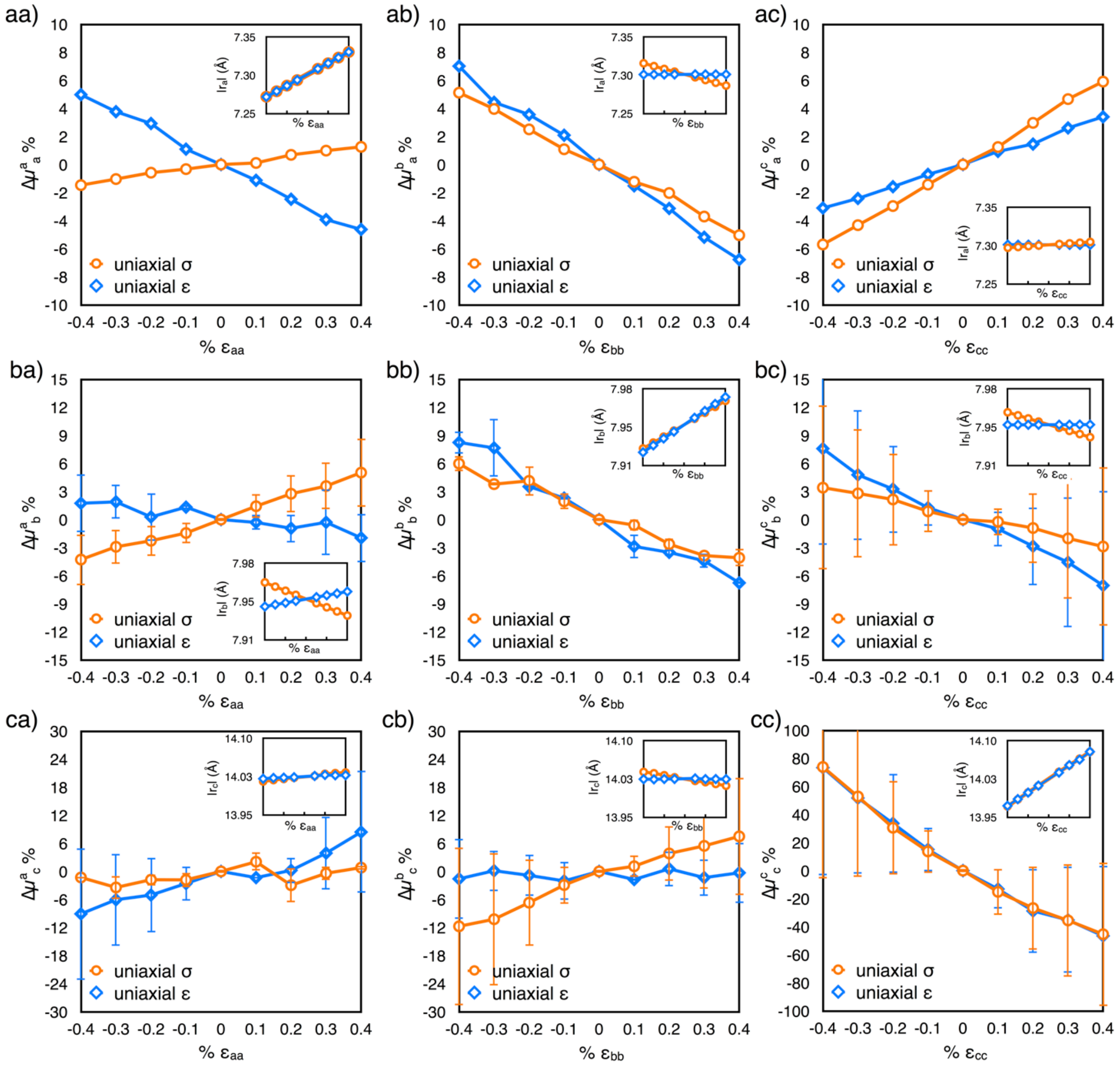

Figure S9 Calculated relative mobility variations $\Delta\mu_i^{\varepsilon}$ as a function of strain magnitude and direction, calculated along the a (top), b (middle), and c (bottom panels) crystal axes. Insets: variation of intermolecular distances $|r_a|$, $|r_b|$, $|r_c|$ between dimers along the same direction of the calculated mobility variation, as a function of strain. Error bars were estimated as the difference between the mobility parallel to the cell vectors and with a misalignment of 5°.

Table S5 Calculated mean $\langle J^t \rangle$, ratio $\langle J^{t2} \rangle / \langle J^t \rangle^2$, standard deviation σ, parameter $\eta = \langle J^t \rangle / \sigma$, skewness and kurtosis of the distributions of electronic couplings shown in Figure S7 *and* Figure S8.

Uniaxial strain

% ε	$\langle J^t \rangle$	$\langle J^{t2} \rangle / \langle J^t \rangle^2$	σ	η	Skewness	Kurtosis
0	94.233	1.084	27.368	3.443	0.507	0.373
% ε_{aa}						
-0.4	97.256	1.086	28.528	3.409	0.582	0.667
-0.3	95.696	1.084	27.757	3.448	0.512	0.391
-0.2	96.419	1.084	27.899	3.456	0.570	0.395
-0.1	94.071	1.087	27.782	3.386	0.521	0.419
0.1	93.408	1.088	27.771	3.364	0.494	0.168
0.2	93.000	1.089	27.787	3.347	0.538	0.220
0.3	92.351	1.087	27.297	3.383	0.488	0.279
0.4	91.489	1.086	26.850	3.407	0.493	0.032
% ε_{bb}						
-0.4	96.842	1.081	27.549	3.515	0.514	0.434
-0.3	96.092	1.084	27.874	3.447	0.555	0.563
-0.2	94.981	1.082	27.168	3.496	0.438	0.010
-0.1	95.206	1.080	26.964	3.531	0.400	0.042
0.1	92.794	1.091	28.034	3.310	0.608	0.669
0.2	93.965	1.088	27.800	3.380	0.519	0.343
0.3	91.830	1.095	28.303	3.244	0.513	0.309
0.4	91.329	1.094	28.023	3.259	0.589	0.852
% ε_{cc}						
-0.4	92.247	1.090	27.649	3.409	0.500	0.222
-0.3	93.498	1.092	28.357	3.448	0.599	0.506
-0.2	94.195	1.089	28.035	3.456	0.555	0.359
-0.1	94.298	1.086	27.599	3.386	0.492	0.329
0.1	94.407	1.087	27.809	3.364	0.499	0.287
0.2	94.795	1.085	27.638	3.347	0.505	0.253
0.3	94.534	1.089	28.237	3.383	0.605	0.558
0.4	94.943	1.089	28.364	3.407	0.599	0.486

% ε	$\langle J_b^t \rangle$	$\langle J_b^{t2} \rangle / \langle J_b^t \rangle^2$	σ	η	Skewness	Kurtosis
0	10.059	1.257	5.098	1.973	0.754	1.104
% ε_{aa}						
-0.4	10.193	1.257	5.164	1.974	0.661	0.570
-0.3	10.188	1.272	5.317	1.916	0.709	0.835
-0.2	10.101	1.264	5.191	1.946	0.760	1.066
-0.1	10.135	1.254	5.106	1.985	0.767	1.038
0.1	10.015	1.268	5.186	1.931	0.756	1.016
0.2	10.048	1.261	5.130	1.959	0.763	0.978
0.3	9.855	1.271	5.132	1.920	0.735	0.828
0.4	9.765	1.272	5.093	1.917	0.623	0.417
% ε_{bb}						
-0.4	10.421	1.250	5.212	1.999	0.742	1.248
-0.3	10.281	1.260	5.242	1.961	0.645	0.564
-0.2	10.268	1.262	5.251	1.955	0.701	0.913
-0.1	10.044	1.264	5.157	1.948	0.664	0.572
0.1	9.956	1.262	5.099	1.952	0.648	0.648
0.2	9.741	1.265	5.019	1.941	0.609	0.300
0.3	9.707	1.268	5.029	1.930	0.721	0.839
0.4	9.692	1.287	5.194	1.866	0.763	0.984

% ε_{cc}						
-0.4	10.167	1.259	5.179	1.974	0.665	0.636
-0.3	10.052	1.260	5.125	1.916	0.642	0.460
-0.2	9.969	1.264	5.119	1.946	0.711	0.828
-0.1	10.063	1.263	5.157	1.985	0.744	1.030
0.1	10.034	1.265	5.165	1.931	0.680	0.782
0.2	10.004	1.263	5.130	1.959	0.708	0.738
0.3	10.049	1.262	5.149	1.920	0.686	0.783
0.4	9.876	1.266	5.089	1.917	0.760	0.909

% ε	$\langle J_c^{t}\rangle$	$\langle J_c^{t2}\rangle/\langle J_c^{t}\rangle^2$	σ	η	Skewness	Kurtosis
0	0.658	1.595	0.433	1.519	0.507	0.373
% ε_{aa}						
-0.4	0.632	1.433	0.415	1.521	1.063	1.798
-0.3	0.648	1.404	0.412	1.574	0.865	1.370
-0.2	0.654	1.401	0.414	1.579	0.822	0.806
-0.1	0.653	1.398	0.412	1.586	0.873	1.032
0.1	0.658	1.393	0.413	1.596	0.833	0.795
0.2	0.658	1.421	0.427	1.542	1.004	1.677
0.3	0.657	1.389	0.410	1.604	0.769	0.514
0.4	0.645	1.440	0.428	1.507	0.969	1.087
% ε_{bb}						
-0.4	0.672	1.392	0.421	1.598	0.884	1.098
-0.3	0.647	1.394	0.406	1.594	0.964	1.856
-0.2	0.661	1.382	0.409	1.617	0.823	0.634
-0.1	0.663	1.412	0.425	1.558	0.998	1.597
0.1	0.638	1.400	0.403	1.581	0.808	0.685
0.2	0.659	1.404	0.418	1.574	0.869	0.934
0.3	0.650	1.411	0.417	1.560	0.920	1.164
0.4	0.650	1.437	0.430	1.512	1.042	1.664
% ε_{cc}						
-0.4	0.746	1.340	0.435	1.521	0.827	1.182
-0.3	0.706	1.393	0.443	1.574	0.934	0.916
-0.2	0.693	1.384	0.430	1.579	0.897	1.530
-0.1	0.674	1.410	0.432	1.586	0.932	1.114
0.1	0.639	1.412	0.410	1.596	0.837	0.711
0.2	0.617	1.428	0.404	1.542	0.975	1.346
0.3	0.602	1.440	0.399	1.604	1.007	1.596
0.4	0.585	1.434	0.385	1.507	0.911	1.138

	Uniaxial stress					
% ε	$\langle J_a^{t}\rangle$	$\langle J_a^{t2}\rangle/\langle J_a^{t}\rangle^2$	σ	η	Skewness	Kurtosis
0	94.233	1.084	27.368	3.443	0.507	0.373
% ε_{aa}						
-0.4	92.719	1.088	27.483	3.409	0.493	0.338
-0.3	94.624	1.084	27.370	3.448	0.468	0.143
-0.2	93.538	1.085	27.287	3.456	0.452	0.068
-0.1	95.322	1.087	28.161	3.386	0.612	0.584
0.1	93.556	1.085	27.258	3.364	0.470	0.136
0.2	93.752	1.088	27.853	3.347	0.615	0.633
0.3	94.687	1.089	28.178	3.383	0.513	0.287
0.4	95.056	1.091	28.629	3.407	0.485	0.374

% ε_{bb}						
-0.4	95.935	1.084	27.862	3.409	0.592	0.647
-0.3	96.010	1.087	28.288	3.448	0.471	0.085
-0.2	95.663	1.088	28.434	3.456	0.534	0.431
-0.1	94.576	1.084	27.346	3.386	0.470	0.279
0.1	93.732	1.090	28.128	3.364	0.574	0.627
0.2	92.380	1.088	27.435	3.347	0.448	0.164
0.3	92.408	1.087	27.215	3.383	0.515	0.271
0.4	92.082	1.089	27.418	3.407	0.483	0.250
% ε_{cc}						
-0.4	92.588	1.093	28.274	3.409	0.616	0.479
-0.3	93.040	1.086	27.339	3.448	0.488	0.263
-0.2	93.117	1.090	27.908	3.456	0.552	0.428
-0.1	93.428	1.084	27.003	3.386	0.467	0.044
0.1	94.756	1.085	27.650	3.364	0.486	0.215
0.2	95.321	1.086	27.883	3.347	0.495	0.348
0.3	95.723	1.088	28.406	3.383	0.515	0.239
0.4	96.576	1.088	28.696	3.407	0.532	0.475

% ε	$\langle J_b^t \rangle$	$\langle J_b^{t2} \rangle / \langle J_b^t \rangle^2$	σ	η	Skewness	Kurtosis
0	10.059	1.257	5.098	1.973	0.754	1.104
% ε_{aa}						
-0.4	9.859	1.272	5.139	1.974	0.695	0.538
-0.3	9.894	1.282	5.252	1.916	0.692	0.678
-0.2	9.956	1.272	5.192	1.946	0.734	0.798
-0.1	9.837	1.270	5.109	1.985	0.752	1.079
0.1	9.955	1.259	5.070	1.931	0.683	0.712
0.2	10.155	1.260	5.182	1.959	0.759	1.014
0.3	10.042	1.278	5.292	1.920	0.764	0.957
0.4	10.044	1.265	5.170	1.917	0.789	1.388
% ε_{bb}						
-0.4	10.216	1.249	5.098	1.974	0.647	0.548
-0.3	10.130	1.252	5.090	1.916	0.678	0.700
-0.2	10.096	1.266	5.212	1.946	0.709	0.850
-0.1	10.109	1.263	5.182	1.985	0.714	0.681
0.1	10.074	1.277	5.303	1.931	0.852	1.460
0.2	9.879	1.283	5.251	1.959	0.742	0.750
0.3	9.891	1.271	5.151	1.920	0.809	1.160
0.4	9.697	1.265	4.991	1.917	0.625	0.403
% ε_{cc}						
-0.4	9.926	1.266	5.118	1.974	0.663	0.488
-0.3	9.998	1.276	5.255	1.916	0.772	0.831
-0.2	10.022	1.274	5.247	1.946	0.714	0.885
-0.1	10.010	1.257	5.074	1.985	0.687	0.764
0.1	10.070	1.260	5.133	1.931	0.708	0.947
0.2	10.070	1.265	5.186	1.959	0.721	0.912
0.3	10.077	1.266	5.198	1.920	0.808	1.224
0.4	10.050	1.263	5.153	1.917	0.743	1.045

$\% \varepsilon$	$<J_c^t>$	$<J_c^{t2}>/<J_c^t>^2$	σ	η	Skewness	Kurtosis
0	0.658	1.595	0.433	1.519	0.507	0.373
$\% \varepsilon_{aa}$						
-0.4	0.649	1.407	0.414	1.521	0.880	1.157
-0.3	0.654	1.415	0.421	1.574	0.878	0.951
-0.2	0.662	1.426	0.432	1.579	1.112	2.514
-0.1	0.652	1.400	0.413	1.586	0.867	1.115
0.1	0.669	1.413	0.430	1.596	1.026	1.762
0.2	0.646	1.404	0.411	1.542	1.014	1.615
0.3	0.665	1.389	0.415	1.604	0.865	0.787
0.4	0.663	1.378	0.408	1.507	0.826	0.944
$\% \varepsilon_{bb}$						
-0.4	0.629	1.409	0.402	1.521	0.862	0.997
-0.3	0.640	1.417	0.413	1.574	0.879	0.788
-0.2	0.630	1.433	0.414	1.579	1.046	1.749
-0.1	0.643	1.429	0.421	1.586	0.960	1.223
0.1	0.657	1.406	0.419	1.596	0.861	0.727
0.2	0.660	1.415	0.425	1.542	1.011	2.093
0.3	0.663	1.403	0.421	1.604	0.914	0.976
0.4	0.661	1.405	0.421	1.507	0.934	1.156
$\% \varepsilon_{cc}$						
-0.4	0.727	1.365	0.439	1.521	0.779	0.595
-0.3	0.702	1.375	0.430	1.574	0.898	1.210
-0.2	0.694	1.390	0.434	1.579	1.035	1.870
-0.1	0.681	1.378	0.418	1.586	0.836	0.968
0.1	0.625	1.439	0.414	1.596	0.961	1.423
0.2	0.612	1.462	0.416	1.542	0.941	1.195
0.3	0.603	1.437	0.399	1.604	0.864	0.878
0.4	0.584	1.440	0.387	1.507	0.951	1.103

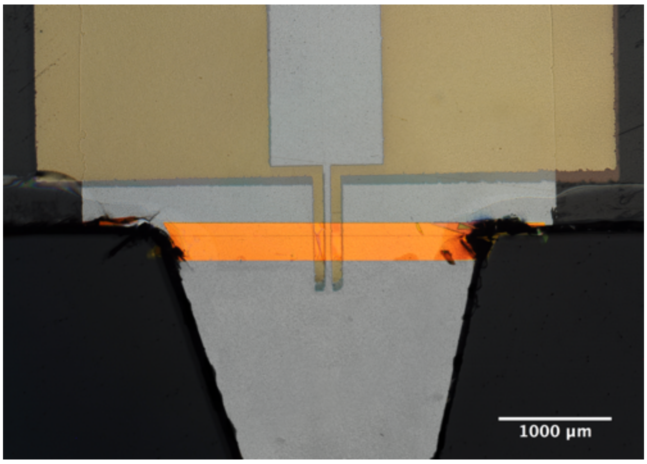

Figure S10 Photograph of a rubrene crystal laminated horizontally on top of a cantilever. It can be seen that how the the crystal is placed near the clamped part of the triangular cantilever in order to obtain a uniaxial strain.

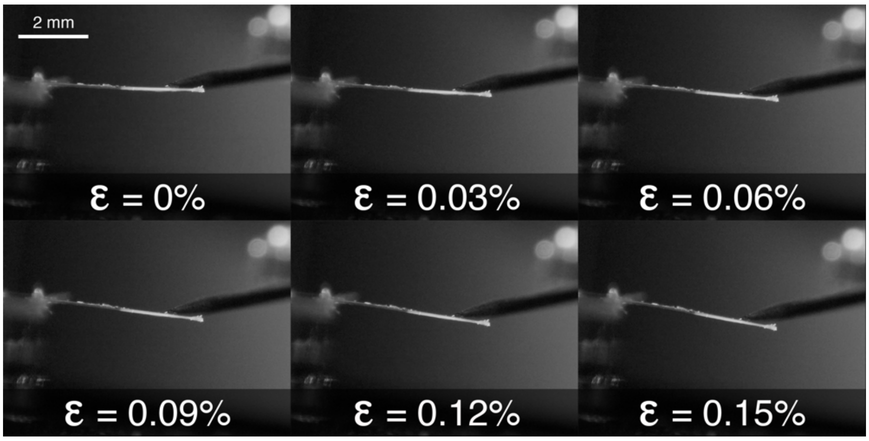

Figure S11 Pictures of the cantilever taken at different tensile strains. The cantilever is the white line in the middle of the picture. The dark shape on the right side of the images is the micromanipulator tip, which applies the force at the free end of the cantilever. The rubrene crystal is laminated on the top of the cantilever, very close to its left end (clamped part in Figure S10).

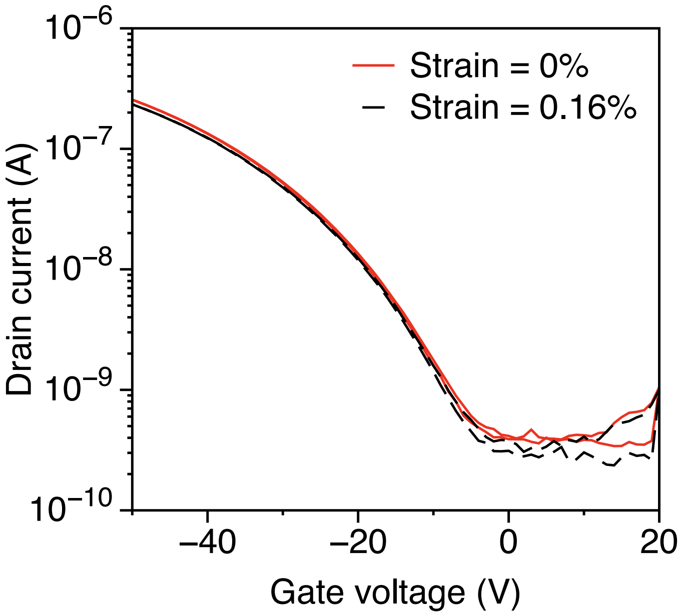

Figure S12 Transfer curves of the rubrene at rest and under a maximal strain of 0.16% at V_{ds} = -50 V.

6. Relation between the relative variations of drain current and mobility

The drain current measured in transistor operating in linear regime (for $V_{ds}<V_{gs}-V_{th}$) can be described by the following equation:

$$I_{d(lin)} = \mu C \frac{W}{L}\left[\left(V_{gs} - V_{th}\right)V_{ds} - \frac{V_{ds}^2}{2}\right] \quad \text{(S4)}$$

For transistor operating in saturation regime ($V_d > V_{gs}-V_{th}$) we have instead:

$$I_{d(sat)} = \frac{1}{2}\mu C \frac{W}{L}\left(V_{gs} - V_{th}\right)^2 \quad \text{(S5)}$$

At fixed source-drain and gate-source voltages, and if the threshold voltage does not change with the applied stress, the first-order relative variation of drain current in both regimes can be written as:

$$\frac{\Delta I}{I} = \frac{\Delta W}{W} + \frac{\Delta C}{C} - \frac{\Delta L}{L} + \frac{\Delta \mu}{\mu} \quad \text{(S6)}$$

where *I* is the drain current, *W* and *L* are respectively the width and the length of the transistor channel, *C* the capacitance and μ the charge mobility.

For both configurations (electrodes placed in the cantilever length direction or in the cantilever width direction), variations of *W* and *L* can be neglected. In fact, in the former case, the variation of *L* will be zero and the variations of *W* small with respect to measured variations of mobility (the variation of *W* is indeed the strain, which is of the order of 0.2% while mobility changes are of the order of 10%). For the second case (electrodes in the cantilever width direction), ΔW will be zero and ΔL small (corresponding to the applied strain). We are then left with:

$$\frac{\Delta I}{I} = \frac{\Delta C}{C} + \frac{\Delta \mu}{\mu} \quad \text{(S7)}$$

Analogously, the relative variation of the capacitance can be written as:

$$\frac{\Delta C}{C} = \frac{\Delta \beta}{\beta} + \frac{\Delta L}{L} + \frac{\Delta w}{w} - \frac{\Delta d}{d} \quad \text{(S8)}$$

with β and *d*, respectively, the permittivity and thickness of the dielectric. Since permittivity and thickness do not change upon strain, and geometrical variations Δw and ΔL can be neglected as explained before, we end up with:

$$\frac{\Delta C}{C} \approx 0 \quad \text{(S9)}$$

Finally, combining equations S7-S10 it emerges how the main variation of drift current upon application of strain, reflects a variation of mobility: $\frac{\Delta I}{I} = \frac{\Delta \mu}{\mu}$ (S10).